Charge Collection Efficiency Characterization of Silicon 3D-Detectors for Microdosimetry

Diana Bachiller-Perea, Javier García López, María del Carmen Jiménez-Ramos, Faustino Gómez, Celeste Fleta, David Quirion, Adrián García-Osuna, and Consuelo Guardiola

***Abstract*—New silicon 3D-microdetectors have been developed to perform microdosimetry measurements for applications in proton therapy. In this work, the charge collection efficiency (CCE) of an improved second generation of microdetectors having two different thicknesses (10 μm and 20 μm) has been studied by means of the ion beam induced charge (IBIC) technique. The results show that, for a silicon volume with a diameter of 25 μm, the CCE is greater than 93 % for the regions at radial distances up to 10 μm from the center of the microdetector, whereas in the regions between 10 μm and 12.5 μm the mean CCE is 75 %. This study will allow us to obtain the CCE characterization for ongoing and further microdosimetry studies in clinical centers.**

***Index Terms*—Microdosimetry, charge collection efficiency, ion beam induced charge, silicon microdosimeters, proton therapy.**

I. Introduction

THE measurement of microdosimetric parameters, such as the lineal energy (y) or the probability density functions $f(y)$, $d(y)$ is of utmost importance to optimize proton therapy treatments since they will determine, among other parameters, the relative biological effectiveness (RBE) of the irradiation [1]. For this purpose, new silicon 3D-microdetectors with size and shape equivalent to those of human cells have been developed and manufactured at the Centro Nacional de Microelectrónica (IMB-CNM, CSIC) in Barcelona, Spain. Their good performance as microdosimeters has already been demonstrated in other works [2], [3].

Because of the importance of a precise determination of the physical parameters involved in the particle-matter interactions for radiotherapy treatments, it is necessary to perfectly characterize the behaviour of our microdevices before their utilization in a clinical context. In this work, the charge collection efficiency (CCE) of the microdosimeters has been studied by means of the ion beam induced charge (IBIC) technique at the microprobe beamline of the Centro Nacional de Aceleradores (CNA, Seville, Spain). Although the devices that we use for the microdosimetry experiments consist of multiple-microdetector arrays, here we have investigated the CCE in the individual cylindrical-cells. The study of the CCE of some 3D-microdetector cells allows for obtaining an average CCE for all the microdetectors of the same dimensions and fabrication processes.

This work was supported by the CNRS-Momentum fellow and the European Union's Horizon 2020 Research and Innovation program under the Marie Sklodowska-Curie Grant Agreement no. 745109 and the G. A. no. 654168.

D. Bachiller-Perea and C. Guardiola are with the Laboratoire de Physique des 2 Infinis Irène Joliot-Curie (IJClab), Centre National de la Recherche Scientifique (CNRS), Université Paris-Saclay, 91405 Orsay, France (e-mail: diana.bachiller-perea@ijclab.in2p3.fr, consuelo.guardiola@ijclab.in2p3.fr).

M. C. Jiménez-Ramos, J. García López, and A. García-Osuna are with the Centro Nacional de Aceleradores and the Departamento de Física Atómica, Molecular y Nuclear, University of Sevilla, 41080, Sevilla, Spain (e-mail: mcyjr@us.es, fjgl@us.es, agosuna@us.es).

F. Gómez is with the Department of Particle Physics, Universidade de Santiago de Compostela and with the Grupo de Imagen Molecular, Instituto de Investigación Sanitaria, 15782 Santiago de Compostela, Spain (e-mail: faustino.gomez@usc.es).

C. Fleta and D. Quirion are with the Instituto de Microelectrónica de Barcelona, Centro Nacional de Microelectrónica (IMB-CNM, CSIC), 08193 Barcelona, Spain (e-mail: celeste.fleta@csic.es, d.quirion@csic.es).

II. Materials and Methods

Fig. 1 shows one of the 11 $\times$ 11 microdetector arrays used for this work, we have studied two arrays with detectors having different thicknesses (10 μm and 20 μm). For these measurements, only one of the 121 microdosimeters composing the array was connected to the readout electronics, and the CCE characterization was carried out in an individual cylindrical-cell. The microdetectors studied here belong to a second and improved fabrication run with respect to those studied in [2], [3]. In particular, the doping process of the electrodes was modified to produce a shallower dopant distribution to achieve a better definition of the active volume. Additionally the critical dimensions of the devices were optimized to increase the fabrication yield. This section describes the structure of the microdetectors and the IBIC technique that has been used to characterize their charge collection efficiency.

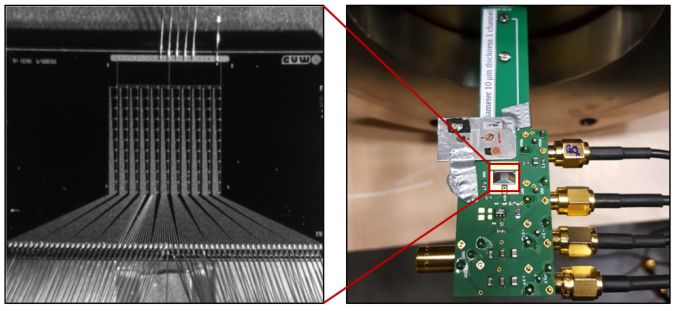

Fig. 1. One of the 11 $\times$ 11 microdetector arrays used for this work. Only an individual dosimeter of the array was connected to the electronics and studied.

A. Silicon 3D-Microdetectors

Two silicon 3D-microdetectors with different thicknesses (10 μm and 20 μm) and an internal diameter of 25 μm (including a n^+ diffusion region right next to the n-doped polysilicon) have been studied in this work. The structure of the unit cell is shown in Fig. 2.

The microdosimeters have been fabricated on silicon-on-insulator (SOI) wafers provided by Icemos Technology Ltd. The sensitive volume of the detector is fabricated in high resistivity ($>$ 3 kΩ·cm) $<$100$>$ n-type doped Si, with 1 μm of buried SiO_2 and 300 μm of low-resistiviy $<$100$>$ Si as support. The p^+-electrode has been fabricated by ionic implantation of boron. Around the 25 μm-diameter cylinder a 3 μm trench is etched, filled with polysilicon (poly-Si), and then doped with phosphorus using $POCl_3$. The P diffuses towards the sensitive volume, creating an n^+ region by diffusion that will act as ohmic contact. A TEOS-based oxide is deposited over the entire surface of the device to create an insulating layer over the P-doped polysilicon. An aluminum line is used to read out the charge collected in the central p^+-electrode, in the multidetector arrays, each Al strip will be connected to an individual channel of a readout chip in order to analyze each microdetector individually. All the n^+-electrodes are connected to a common contact by aluminum lines. Finally, a SiO_2/Si_3N_4 passivation bilayer is deposited over the whole surface. More information about the fabrication process can be found in [2], [4].

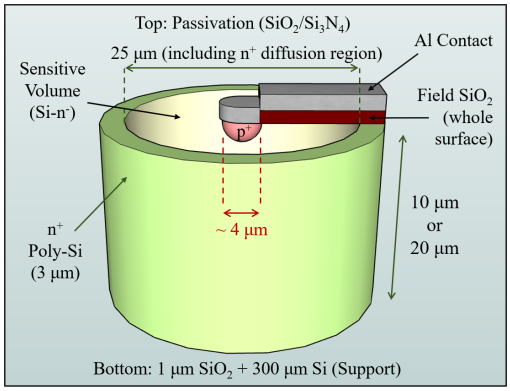

Fig. 2. Sketch and dimensions of the 3D-microdetector structure.

The orientation of the microdosimeters during the experiments is indicated in Fig. 3. As we will see in the experimental results, it is important to take into account the orientation of the detectors (especially, the position of the Al contact line connected to the p^+-electrode) because it will explain some of the effects observed during the IBIC measurements.

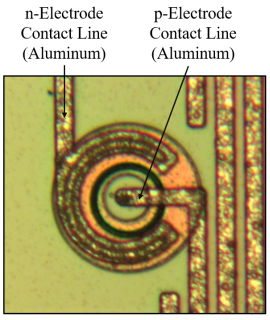

Fig. 3. Optical image of the top view of a microdetector indicating its orientation during the experiment (seen from the beam direction).

B. IBIC Technique

The IBIC technique is a scanning microscopy technique in which MeV ion beams are used as probes to image electronic properties of semiconductor devices [5]. In this work, we have studied the CCE of the 3D-microdetectors by irradiating with He^{2+} ions of a few MeV, which produce electron-hole pairs in the sensitive volume (SV) of the detector. The charge generated in the SV is collected by the electrodes and the p^+-electrode signal is read out and preamplified on the own electronic board of the detectors. In the experimental set-up at the CNA's microprobe facility, the detectors were placed in a vacuum chamber and their output signal was transmitted to an electronic chain consisting of an amplifier, an Analog to Digital Converter (ADC), and the OMDAQ data acquisition system from Oxford Microbeams. The ion beam was rastered over an area of 50 μm $\times$ 50 μm performing a scan of 256 $\times$ 256 steps (195 nm/step) with a dwell time of 10 μs/step. The signal produced by the detector was recorded in an event-by-event mode. The synchronization between the DAQ system and the beam raster system allowed us for correlating each recorded event of the full energy spectrum (the energy of the event, and therefore, the CCE related to that event) to the position of the microdetector (divided in 256 $\times$ 256 pixels with size 0.2 μm $\times$ 0.2 μm) in which the event is produced. We have divided the region of the energy spectrum having events in 50 regions of interest (ROIs) with the same number of ADC channels (16 or 17 depending on the detector). For each ROI, we record the number of counts measured by each of the 256 $\times$ 256 pixels, thus forming 50 CCE maps, each covering a $\sim$ 2 % CCE interval.

The energy of the He^{2+} ions was 3.5 MeV for the 10 μm-thick microdetector and 5.0 MeV for the 20 μm-thick one, depositing an energy in the SV of $\sim$ 2.5 MeV and $\sim$ 4.2 MeV, respectively (calculated with SRIM [6]). Both energies were chosen in order to have an ion range larger than the thickness of the detectors, so they will produce electron-hole charge carriers all along the depth of the device. In both measurements the bias voltage was +10 V, the ion flux $\sim 4 \times 10^7$ $s^{-1}cm^{-2}$, and the acquisition time $\sim$ 30 min.

In order to estimate the beam size, a copper grid with 5 μm-thick wires and a distance of 25 μm between wires has been used. Fig. 4 shows the image obtained detecting the X-rays from the L transitions of the Cu with a Si(Li) detector when the 5.0 MeV He^{2+} beam is rastered over an area of 100 μm $\times$ 100 μm. This measurement will be only an estimation and a maximum value of the beam size because, in order to avoid irradiation damage of the detector during the IBIC analysis [7], the object slits are almost completely closed to drastically reduce the ion rate to a few hundred ions·s^{-1}. A detailed study of the radiation hardness of these microdosimeters against ion irradiation is beyond the scope of this article and will be published in a separate article. Although the exact size of the beam will be determined from the experimental results, the measurements with the copper grid give us an idea of the beam size and prove that the scan size is correct.

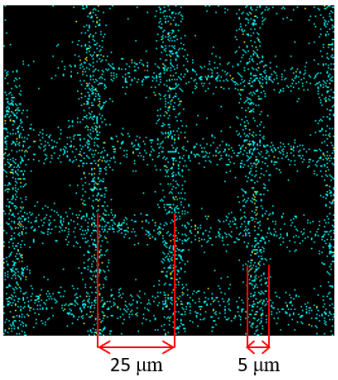

Fig. 4. 100 μm $\times$ 100 μm scan of a copper grid to estimate the beam size.

The ion beam has a Gaussian distribution in both X and Y directions, the full width at half maximum (FWHM) measured with the copper grid (before reducing the beam with the slits) was 3.2 μm $\times$ 4.1 μm for the 10 μm-thick detector, and 3.2 μm $\times$ 3.6 μm for the 20 μm-thick detector. These values correspond to standard deviations (σ_x, σ_y) of 1.4 μm $\times$ 1.8 μm and 1.4 μm $\times$ 1.5 μm, respectively for the 10 μm and the 20 μm-thick detectors.

III. Results

Fig. 5 shows the energy spectrum obtained with the 10 μm-thick detector with 3.5 MeV He^{2+} ions. We have selected five regions (R1-R5) of the spectrum to show the areas of the device in which the events of those regions have been originated. The main peak (R4) centered in channel 776 corresponds to the energy loss of the 3.5 MeV He^{2+} ions in the sensitive volume of the device, and the counts of this peak come mainly from the central region of the SV not having the Al layer on top of it. A complete charge collection is assumed here because the distance that the created electron-hole charge carriers have to travel to reach the electrodes is much shorter than their drift length: a few tens of μm vs. several cm, considering an average electric field of $\sim 10^4$ V/cm and a carrier's lifetime of $\sim$ 1 μs. Therefore, the centroid of the main peak (channel 776 in this case) corresponds to a CCE of 100 %. The low-energy events (R1 and R2) are originated in the external region of the detector. In R3 we observe events with a lower energy than the main peak coming from a small central area of the dosimeter, this is due to the p^+-electrode, because the charge generated within the electrode will not fully contribute to the measured signal. The small peak at higher energy (R5) corresponds to the particles impinging on the area having the Al contact line, the He^{2+} ions will deposit a higher energy in this region than in the region of the detector without Al.

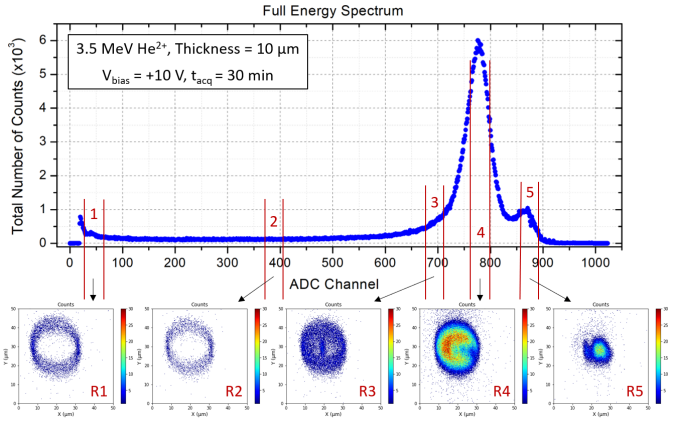

Fig. 5. Energy spectrum obtained with the 10 μm-thick microdetector and regions of the detector where the events are produced.

The same analysis has been done for the spectrum obtained with the 20 μm-thick detector and 5.0 MeV He^{2+} (Fig. 6). The same effects than before are observed, but in this case we cannot distinguish the peak of the events detected in the Al contact line region because the difference between the energy deposited here with respect to the main peak is lower than the difference for the 10 μm-thick detector. However, we can observe the area with the metal in R5.

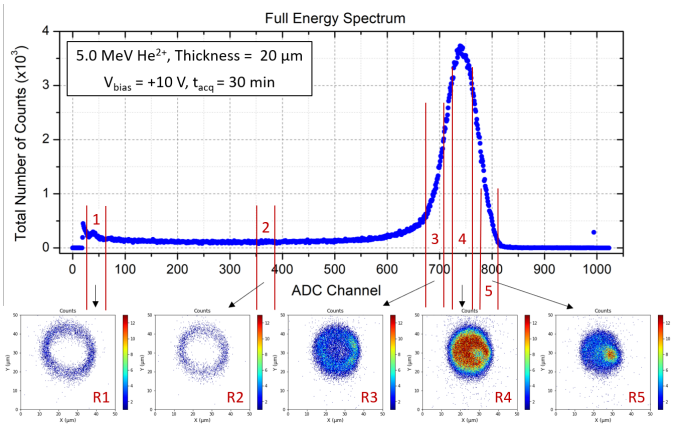

Fig. 6. Energy spectrum obtained with the 20 μm-thick microdetector and regions of the detector where the events are produced.

Both spectra had very low noise, allowing us for measuring the spectra from channel 27 which, compared to the channels of the main peaks (776 and 746, respectively), corresponds to a CCE of $\sim$ 3.5 %.

We have calculated the beam size by analyzing individually more than 30 of the 50 ROIs of the energy spectrum (described in section II-B). We have selected the ROIs before the main peak of the spectrum to obtain the images of the "rings" near the edge of the detector. By fitting the profiles of the number of counts in the rings with Gaussian functions, as shown in Fig. 7, we can calculate the beam size. We have calculated the beam size only in the horizontal direction (X) because we have observed a slight drift of the beam in the vertical direction (Y) during the measurements, provoking a higher dispersion of the experimental data in this direction and making it complicated to correctly fit with the Gaussian peaks. For the X-size we have

fitted both sides of the rings (left and right) in 33 and 35 ROIs for the 10 μm and the 20 μm-thick detectors, respectively, and we have calculated the beam size with the average of all the fits obtaining $\sigma_x = (0.68 \pm 0.11)\ \mu m$ for the 10 μm-thick detector and $\sigma_x = (1.34 \pm 0.14)\ \mu m$ for the 20 μm-thick detector. Knowing the size of the beam in the X-direction, we will be able to estimate σ_y later with a different method, but because the vertical drift of the beam we will focus more in the analysis of the X-direction, which is representative of the dosimeter behavior since it has a cylindrical symmetry.

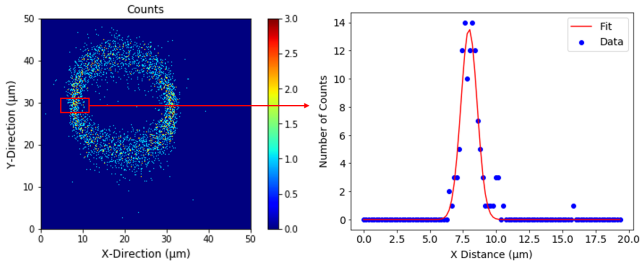

Fig. 7. Gaussian fit of the external ring to calculate the beam size.

A. Active Volume of the 10 μm-Thick Microdetector

Before studying the CCE, we have calculated the active volume of the detectors by analyzing their intrinsic efficiency in different regions of the detector. The intrinsic efficiency is defined as the ratio between the number of pulses recorded and the number of particles incident on the detector (independently of the energy with which they are measured) [8]. Fig. 8 shows the 3D distribution of the total counts recorded by the detector during the measurement. The central region of the detector counts the maximum number of events which decays to zero near the borders of the dosimeter as a result of the convolution between the intrinsic efficiency of the detector and the Gaussian beam.

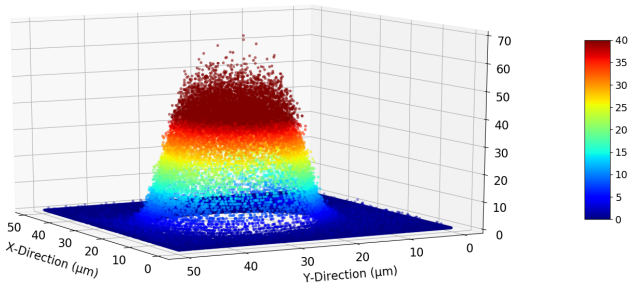

Fig. 8. 3D of the total number of events detected by the 10 μm-thick microdetector.

In order to reproduce the experimental data we have convolved the 2D Gaussian beam (Fig. 9a) with a 2D function that considers a 100 % intrinsic efficiency within a radius r_{eff} and 0 % outside this radius (Fig. 9b). The result of the 2D convolution is shown in Fig. 9c, and the experimental data are shown in Fig. 9d (both normalized to the mean value of counts in the central region of the detector). During this measurement, we observed a vertical shift of the ion beam, we have simulated this shift by using a beam with a higher σ_y than the actual one. The X-profiles indicated by a red horizontal line in Figs. 9b, 9c, and 9d are shown in Fig. 10 for an easier and more precise comparison.

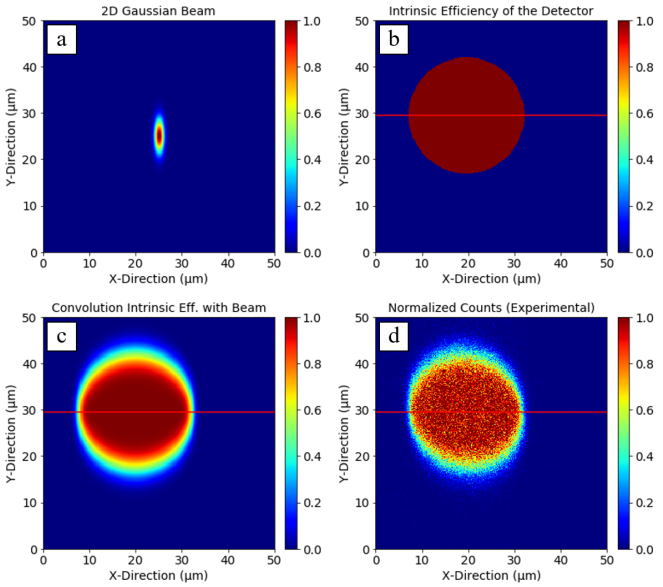

Fig. 9. (a) 2D Gaussian beam. (b) Intrinsic efficiency of the 10 μm-thick microdetector. (c) 2D convolution of the intrinsic efficiency with the Gaussian beam. (d) Experimental data of the total number of counts detected (normalized to the mean value of the plateau).

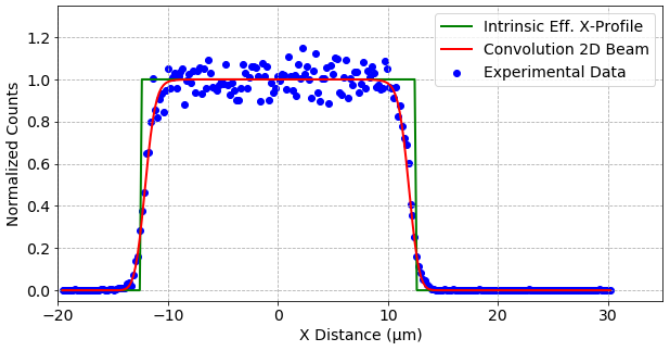

Fig. 10. X-profiles of the intrinsic efficiency, of its 2D convolution with the beam, and of the measured number of counts for the 10 μm-thick detector (normalized to the mean value of counts in the plateau).

By fitting the 2D convolution profile to the experimental data (Fig. 10) we can determine the value of r_{eff} and the beam size (which has been cross-checked with the method explained in Fig. 7). The results obtained are:

$$\sigma_x = (0.68 \pm 0.12)\ \mu m$$

$$\sigma_y = (2.54 \pm 0.20)\ \mu m$$

$$r_{eff} = (12.11 \pm 0.16)\ \mu m$$

$$\varnothing_{eff} = (24.22 \pm 0.32)\ \mu m$$

These values indicate that the 10 μm-thick microdetector has an intrinsic efficiency of 100 % in the regions closer than

12.1 μm from the center: we detect all the particles arriving in those regions of the detector. The regions at distances larger than 12.1 μm will have a CCE < 3.5 % which is the level of noise in our spectrum, and therefore, we can consider they have a null intrinsic efficiency: we cannot measure the particles arriving in those regions. We can conclude that the effective diameter of the 10 μm-thick detector is (24.22 $\pm$ 0.32) μm, which corresponds to an active volume of (93.9 $\pm$ 0.6) %.

Although the fit of the convolution of the intrinsic efficiency with the beam is practically unambiguous (since we know the beam size), we will verify later with an alternative method (in Section III-C1) that the intrinsic efficiency in the region next to the edge of the detector is, indeed, 100 %.

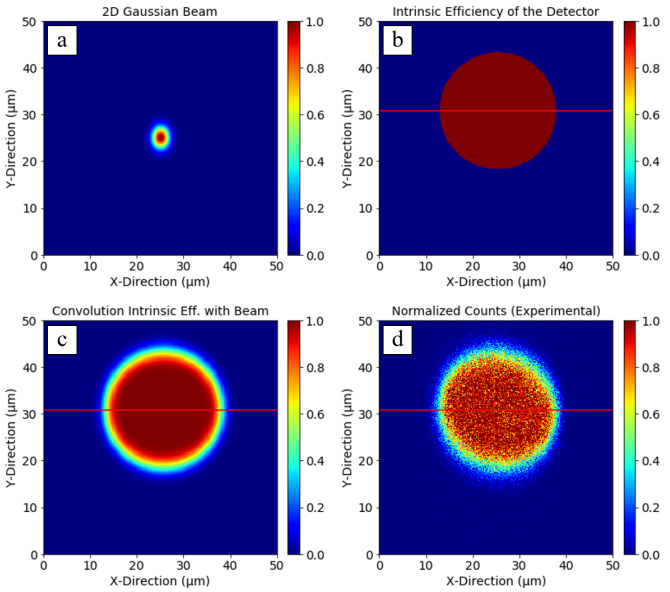

Fig. 12. (a) 2D Gaussian beam. (b) Intrinsic efficiency of the 20 μm-thick microdetector. (c) 2D convolution of the intrinsic efficiency with the Gaussian beam. (d) Experimental data of the total number of counts detected (normalized to the mean value of the plateau).

B. Active Volume of the 20 μm-Thick Microdetector

The same analysis has been done for the 20 μm-thick detector. Fig. 11 shows the 3D distribution of the total counts.

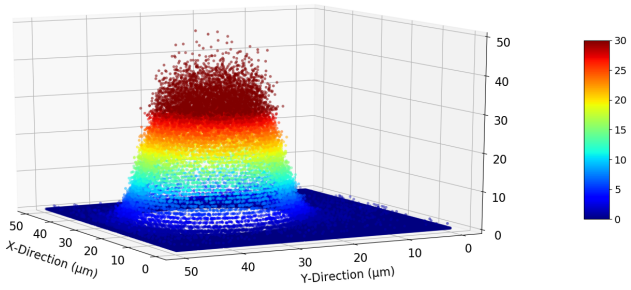

Fig. 11. 3D of the total number of events detected by the 20 μm-thick microdetector.

The 2D convolution of the beam and the intrinsic efficiency, as well as the experimental data (normalized number of counts) are shown in Fig. 12. In this case, we did not have any beam shift during the measurement and the calculated beam size is the actual one (Fig. 12d). The beam is larger in the X-direction than the one used for the previous detector.

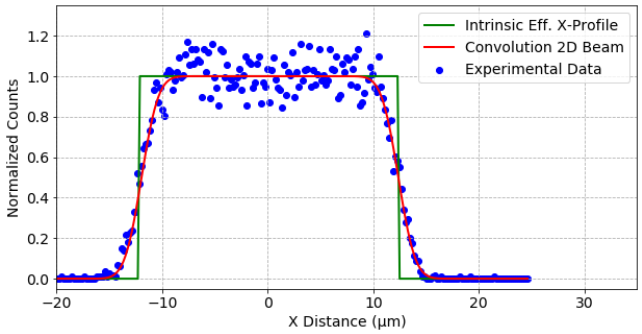

Fig. 13. X-profiles of the intrinsic efficiency, of its 2D convolution with the beam, and of the measured number of counts for the 20 μm-thick detector (normalized to the mean value of counts in the plateau).

Fig. 13 shows the experimental and the calculated X-profiles of the intrinsic efficiency. The beam size and the results obtained from this fit are the following:

$$\sigma_x = (1.25 \pm 0.12)\ \mu m$$

$$\sigma_y = (1.64 \pm 0.12)\ \mu m$$

$$r_{eff} = (12.26 \pm 0.16)\ \mu m$$

$$\varnothing_{eff} = (24.52 \pm 0.32)\ \mu m$$

We obtain an effective diameter of the 20 μm-thick detector slightly larger than the 10 μm-thick detector one. The corresponding active volume is (93.9 $\pm$ 0.6) %.

C. CCE of 10 μm-Thick Microdetector

The charge collection efficiency (CCE) has been calculated for each of the 256 $\times$ 256 pixels as the weighted average CCE using Eq. 1.

$$\overline{\text{CCE}}\ (\%) = \frac{\sum_{i=1}^{50} n_i Channel_i}{N_T Channel_{peak}} \times 100 \qquad (1)$$

Where n_i is the number of counts for that pixel in each of the 50 ROIs of the energy spectrum described in section II-B, $Channel_i$ is the central ADC channel (proportional to the energy collected) of the ROI, N_T is the total number of counts in the spectrum, and $Channel_{peak}$ is the channel of the center of the main peak. Throughout all this work, the values of the CCE for each pixel have been normalized to the centroid of the main peak (which, as previously explained, corresponds to a CCE of 100 %) and expressed in %. From now on, we will refer to these values as the measured CCE. In order to reduce the noise for the calculations, we have set the condition of having a minimum of 5 counts in the pixel to be considered for the analysis.

The 3D distribution of the measured CCE for the 10 μm-thick microdetector is shown in Fig. 14. We observe that in the central region we are measuring a 100 % of CCE, which decreases as the radial distance increases as a result of the convolution of the real CCE of the detector and the Gaussian beam. It is important to mention, and we will recall it later, that when part of the beam is outside the active volume of the device, the particles which are not inside the effective radius will not contribute to the energy spectrum (because the intrinsic efficiency there is null) and, therefore, will not contribute to the calculation of the CCE (Eq. 1). The effect that this will produce is that in the regions of the detector where an important fraction of the beam is impinging outside the SV, the values measured for the CCE will be higher than the real ones and also higher than the values that we can obtain by implementing a standard convolution in which we will consider zero values outside the detector. For the same reason, we have regions outside the detector whose real CCE is zero (since they are outside the active volume) but in which we will measure a higher CCE because part of the beam is touching the active volume of the detector and will produce a signal in the energy spectrum.

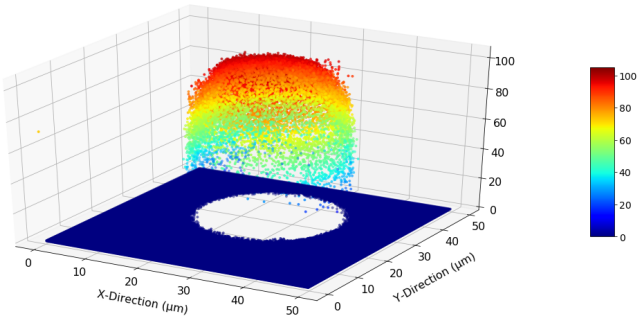

Fig. 14. 3D distribution of the measured CCE for the 10 μm-thick microdetector.

Fig. 15 shows the measured 2D CCE-map and the CCE profiles obtained from the map in the vertical direction (Y, top) and the horizontal direction (X, bottom). The profiles have been calculated doing the average of three columns/rows to have better statistics. The Y-profile shows a higher dispersion because of the vertical drift of the beam during the measurement. In the X-profile, one can observe the region of the central electrode with a lower CCE since the charge generated here is not fully collected. We observe also the region of the Al contact having, apparently, a CCE $>$ 100 % because the ions lose some energy when going through the metal and, therefore, deposit a higher energy in the regions with Al than in the regions without it. The points at higher distances than the effective radius (12.1 μm) are, as explained before, due to the non-negligible beam size, which is still impinging on the active volume of the detector even if its central position is outside the SV.

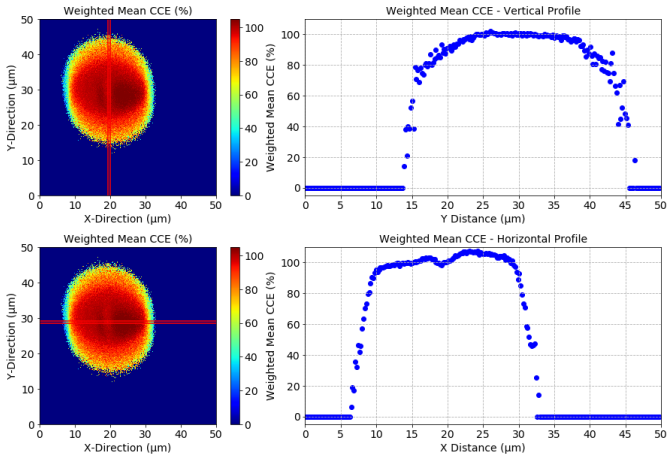

Fig. 15. Left: 2D map of the CCE for the 10 μm-thick microdetector. Right: CCE profiles in the vertical (top) and horizontal (bottom) directions as indicated by the red lines in the 2D maps.

Until now we have shown the values of the measured CCE, which result from the 2D convolution of the actual CCE with the beam; but the goal is to determine the real CCE of the dosimeters. We have calculated the real CCE in three steps: 1) Calculation of the CCE as a function of the radial distance comparing two different methods, 2) Fit of the 2D convolution with the beam to determine the apparent CCE in the central electrode and the Al region, and 3) Correction of the apparent CCE in the central electrode.

1) Radial dependence of the CCE: The CCE in each point of the detector depends on its distance to the central electrode (i.e., on its radial distance to the center of the device and its depth), as has been studied in [3]. In our study, both 3.5 MeV and 5 MeV He^{2+} ions have a larger longitudinal range than the detector thickness, and the trajectories of the ions are perpendicular to the surface of the detector, which means that the ions with produce electron-hole pairs all along the depth of the device. Therefore, we can consider that the detectors are formed by concentric cylinders, each of them having a certain CCE that will decrease as the radial distance from the cylinder to the central electrode increases. We can observe this effect in the ROI maps in Figs. 5 and 6 (excepting the region of the detector having aluminum). We have calculated the CCE as a function of the radial distance with two different methods and we have verified that both of them give the same result.

a) Method A: using the maps of the ROIs.

As we explained before we have 50 2D CCE maps corresponding to 50 regions of the energy spectrum. The analysis of the maps indicates that the CCEs corresponding to the low channels are distributed in a series of rings located around the centre of the detectors, whose radius increases slowly as the CCE decreases, until the limit of the active zone of the dosimeter is reached. To determine the curve "Real CCE vs. radial distance" we have calculated for all the ROIs before the centroid of the main peak, the radial distance of the pixels at which we observe the counts in that ROI. This have been calculated as we saw in Fig. 7, but now measuring the distance between the centers of the left and the right sides of the ring and dividing by 2. As we approach to the center of the main peak, we observe wider regions of the detector counting, for these cases, we have considered the central position of the region. The CCE value assigned to each radial distance is the mean CCE corresponding to that ROI: the central channel of the ROI divided by the channel of the center of the main peak and expressed in %. The results obtained with this method will be compared later to the results obtained with Method B.

Since the beam scan is homogeneous, this characteristic of the detectors with cylindrical regions of different CCE has to be reflected in the number of measured counts in the total energy spectrum. For example, if we consider the annulus between $r_{eff} = 12.11\ \mu m$ and an internal radius $r_{in} = 11.22\ \mu m$, one can compare the percentage of the total volume (V_T) corresponding to the cylinder defined by this annulus and the thickness of the detector to the percentage of counts in the spectrum corresponding to this interval of CCEs (Fig. 16). Both r_{in} and its CCE value come from the calculation made with the ROI maps.

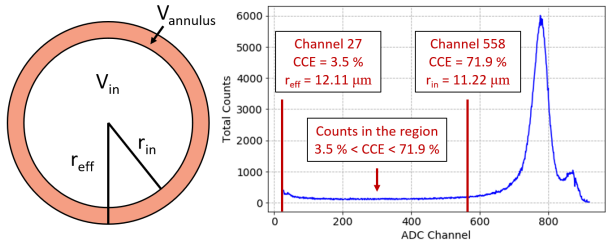

Fig. 16. $V_{annulus}$ is the volume of the cylinder defined by the annulus between r_{in} and r_{eff} and the thickness of the detector. V_{in} is the volume of the cylinder defined by r_{in} and the thickness of the detector. Therefore: $V_{annulus} = V_T - V_{in}$. The red bars on the spectrum indicate the counts originated in the volume $V_{annulus}$.

The percentage of the total volume occupied by the cylinder defined by this annulus is 14 %:

$$\frac{V_{annulus}}{V_T} = 1 - \frac{V_{in}}{V_T} = 1 - \frac{r_{in}^2}{r_{eff}^2} = 0.14 \tag{2}$$

And the percentage of number of counts in the region of the spectrum corresponding to the cylinder is also 14 %:

$$\frac{\text{Counts (3.5 \% - 71.9 \%)}}{N_T} = \frac{73935}{529995} = 0.14 \tag{3}$$

Where N_T is total number of counts in the energy spectrum.

This is an alternative method to verify that in the region next to the edge of the detector, the intrinsic efficiency is 100 %, as seen in Section III-A.

b) Method B: using the energy spectrum.

As we have seen, since all points of the dosimeter have been irradiated with the same amount of ions, the fraction of the detector volume with a certain CCE is related to the number of counts in the energy spectrum through the following formula:

$$\frac{V_i}{V_T} = \frac{N_i}{N_T} \tag{4}$$

Where V_i is the volume of the cylinder defined by a radial distance r_i, V_T is the total volume of the detector, N_i is the number of counts between channel i and the end of the spectrum, and N_T is the total number of counts in the spectrum. This expression can be easier understood with Fig. 17.

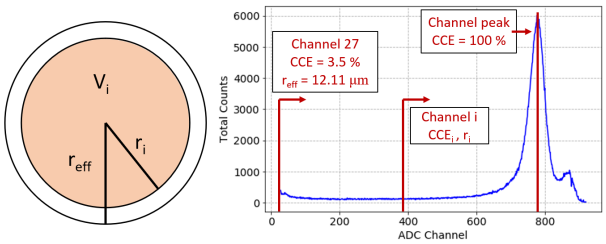

Fig. 17. Region of the spectrum originated in the cylindrical volume of the detector with $r < r_i$.

Therefore, the radial distance related to each channel in the spectrum can be calculated as:

$$r_i = \sqrt{\frac{\sum_{j=i}^{peak} n_j}{N_T}} \times r_{eff} \tag{5}$$

Where n_j is the number of counts in channel j.

And the CCE associated to the radial distance r_i is calculated as:

$$\text{CCE (\%)} = \frac{\text{Channel i}}{\text{Channel peak}} \times 100 \tag{6}$$

Whereas in the low CCE region of the spectrum (i.e., before the main peak) we can easily calculate the pairs of values r_i, CCE_i, for the region of the main peak we have to correct the spectrum in order to correctly calculate the fraction of counts corresponding to each r_i. Since the main peak is approximately symmetrical (except for the Al region), we can do this correction by adding to each channel of the main peak on the left of the centroid the number of counts in the symmetrical channel with respect to the centroid, as shown in Fig. 18 (red line). In the case of the 10 μm-thick detector, the main peak is not symmetrical because of the counts coming from the Al region, we have calculated the corrected spectrum in a second way, multiplying by two the number of counts in each channel of the main peak on the left of the centroid (green line in Fig. 18) to eliminate the Al-region contribution. Once we have corrected the spectrum we can calculate the pairs of values r_i, CCE_i appliying Eqs. 5 and 6.

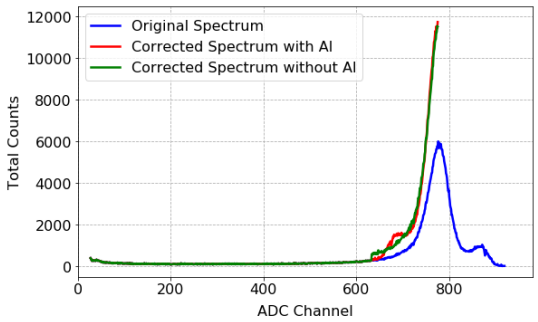

Fig. 18. Blue: Original spectrum. Red: Corrected spectrum including the counts from the Al region. Green: Corrected spectrum excluding the counts from the Al region.

The results obtained with both methods (A and B), and in the case of B including and excluding the counts from the Al region, are compared in Fig. 19. The blue dots correspond to the measured CCE (measurement of the X-profile averaging the left and right sides). This plot (the blue dots) shows very clearly the effect explained at the beginning of this section: the CCE values measured near the edge and outside the detector are higher than the real ones as a consequence of the particular convolution with the beam, in which the points outside the detector do not contribute as zeros to the calculation of the CCE. We had calculated in section III-A the active volume of the detector, which ends at a radial distance of 12.1 μm. As can be seen, the agreement between both methods (in Fig. 19: A in orange, B in blue and red) is very good not only for low CCE values, where we have ring-shaped maps, but also for the rest of the detector. The fact of including (red) or excluding (blue) the counts from the Al region does not affect our result significantly (even in this extreme case of the 10 μm-thick detector). Since both methods are compatible, we have chosen Method B for the calculation of the real CCE since it has a better resolution (around 700 points against 50 in Method A).

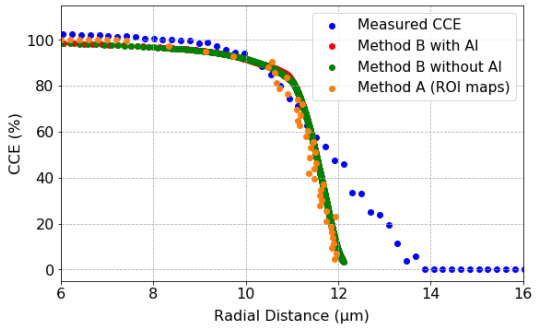

Fig. 19. Blue: Measured values of the CCE. Red: CCE calculated with Method B including the Al region. Green: CCE calculated with Method B excluding the Al region. Orange: CCE calculated with Method A.

The model in Method B, which is basically limited by the minimum CCE we can measure above the electronic noise, allows us to study the distal region of the detector more robustly than through the analysis of the maps, with the huge advantage that the results are practically independent on the beam size. As an example, Fig. 20, shows the results of applying the model to two different spectra obtained for the 20 μm-thick detector with 5 MeV He^{2+} ($\sigma_x = 1.3\ \mu m$) and 8 MeV He^{2+} ($\sigma_x = 2.5\ \mu m$) (this second measurement has not been included in this work but we use it here for comparison), where it is apparent that the two spectra produce the same radial CCE (note that both ions have an ion range larger than 20 μm, producing charge carriers over the full thickness of the detector).

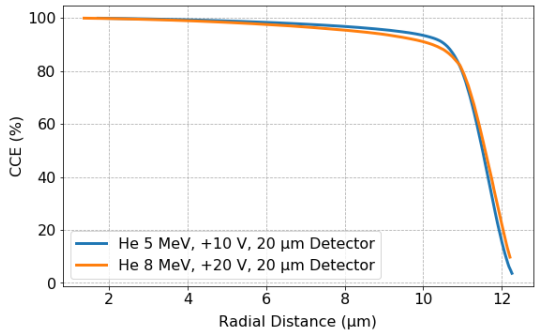

Fig. 20. CCE calculated with Method B for the 20 μm-thick detector with two different beams (different energy and beam size).

2) Fit of the 2D convolution with the beam: Once we have the values of the CCE as a function of the radius, we can use the 2D convolution of the calculated CCE with the 2D Gaussian beam to verify that the calculation of the CCE is correct and to calculate the apparent CCE in the regions with aluminum and in the central electrode by fitting the X-profile of the 2D convolution. We can determine the limits where the convolution should stop working by comparing the size of the detector and the beam (Fig. 21). For the 10 μm-thick detector the convolution should only work until $r \approx 9\ \mu m$ in the X-direction and until $r \approx 4\ \mu m$ in the Y-direction.

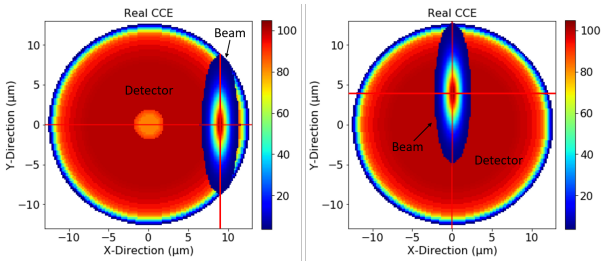

Fig. 21. Comparison of the beam and the detector sizes to determine the region where the convolution works.

To study the central region of the detector, we have reproduced in 2D the real CCE with the values calculated with Method B (because of the cylindrical symmetry of our detector). We have reproduced also the shape of the central electrode, with a border of Al slightly larger than the electrode, and the shape of the Al contact line (remember Fig. 2). The real CCE in 2D and its horizontal profile are shown in Figs. 22a and 22b. We have convolved the calculated CCE with the 2D Gaussian beam (beam in Fig. 9a), the result of the 2D convolution is shown in Fig. 22c. Comparing to the measured CCE map (Fig. 22d), we see that the borders are not well reproduced as expected since we are convolving with

values of zero outside the detector, but the central region of the detector is well reproduced.

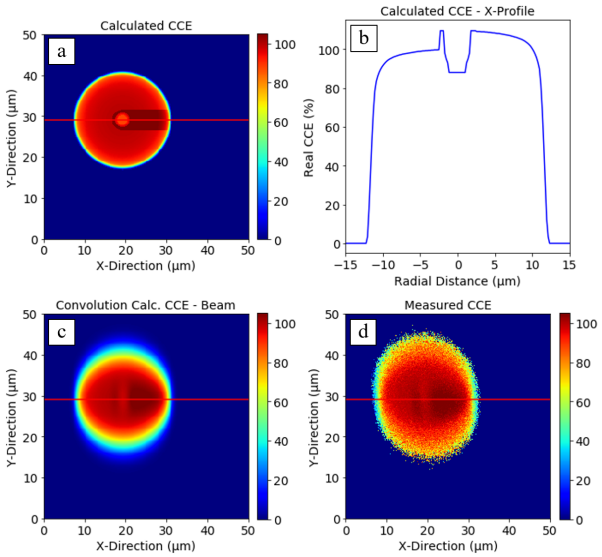

Fig. 22. (a) Calculated CCE of the detector in 2D. (b) X-profile of the calculated CCE. (c) 2D convolution of the calculated CCE with the Gaussian beam. (d) Measured CCE.

We have fitted the 2D convolution to the experimental data by using the horizontal profile (Fig. 23) to calculate the apparent value of the CCE in the regions with Al and in the central electrode. As explained before, our convolution is lower than the experimental data in the borders, this is why the interest of this convolution is only to study the central region of the dosimeter. The value that we have to use in the region of the Al contact line and the borders of the central electrode (which also have Al) to simulate the higher energy deposited there is 109.5 %. For the electrode we have defined four concentric regions with different CCE, the external diameter is 3.6 μm and the CCE decreases from 98 % in the border to 88 % in the center.

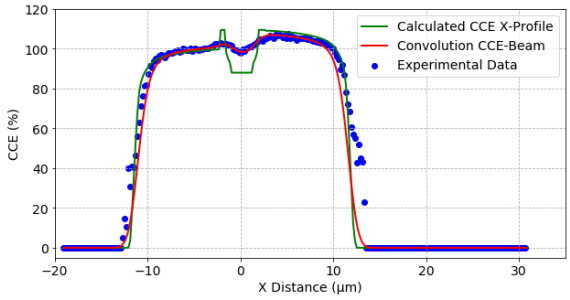

Fig. 23. X-profiles of the measured CCE, the calculated CCE, and the 2D convolution of the calculated CCE with the beam for the 10 μm-thick microdetector.

3) Correction of the central electrode: With the 2D convolution we have calculated the apparent CCE in the central electrode. Since we also have Al on top of the electrode, the real value of the CCE there is lower because the deposited energy is higher than in the regions without Al. Since we know that in the borders of the electrode the apparent CCE was 109.5 % instead of 100 %, we can calculate the real CCE in the electrode region, which goes from 89.5 % in the edge to 80.4 % in the center (in four concentric regions starting from $r = 1.8\ \mu m$).

After applying the steps 1), 2) (with Method B), and 3), we are able to reconstruct the real CCE of the 10 μm-thick detector in 2D. The result is presented in Fig. 24.

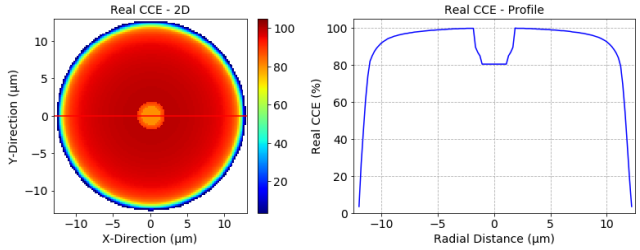

Fig. 24. Real CCE of the 10 μm-thick microdetector.

D. CCE of the 20 μm-Thick Microdetector

The study of the 20 μm-thick detector is analog to the one we have made for the 10 μm detector, we have followed exactly the same steps. Fig. 25 shows the 3D distribution of the measured CCE.

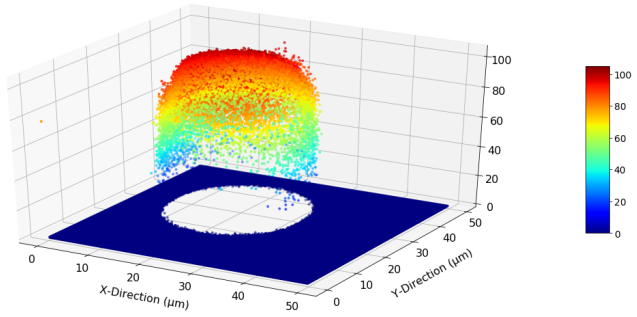

Fig. 25. 3D of the CCE measured for the 20 μm-thick microdetector.

The 2D CCE-map and the vertical and horizontal profiles are shown in Fig. 26. Also in this case we have a higher dispersion in the vertical direction because σ_y of the beam was larger than σ_x. For this detector (20 μm-thick), and with the 5.0 MeV He^{2+} ions, the difference of the energy loss in the Al contact line is lower than in the 10 μm-thick detector, therefore, the Al contact line is less evident than before in the X-profile. For the same reason, the central electrode is practically not visible in this profile.

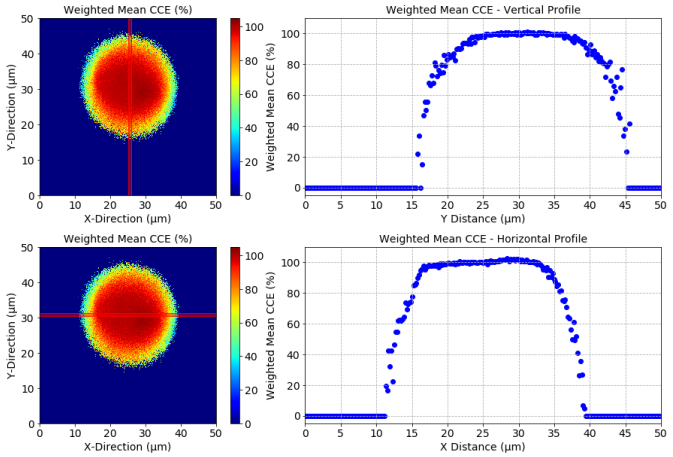

Fig. 26. Left: 2D map of the CCE for the 20 μm-thick microdetector. Right: CCE profiles in the vertical (top) and horizontal (bottom) directions as indicated by the red lines in the 2D maps.

1) Radial dependence of the CCE: As for the 10 μm-thick detector, we have calculated the CCE as a function of the radial distance of the concentric cylinders using Method B (calculation from the number of counts in the spectrum), and we have reproduced the calculated CCE in 2D. We already showed the result of this calculation in Fig. 20.

2) Fit of the 2D convolution with the beam: Fig. 27 shows that, for this detector, the convolution of the calculated CCE with the beam should only work until $r \approx 8\ \mu m$ in the X-direction and until $r \approx 7\ \mu m$ in the Y-direction (the beam size is different than the one in the previous case).

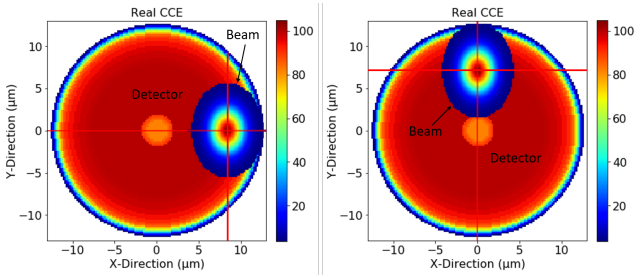

Fig. 27. Limits at which the 2D convolution works for the 20 μm-thick detector.

Fig. 28 shows the calculated CCE in 2D (a), its profile (b), the 2D convolution of the calculated CCE with the beam (c), and the measured CCE 2D-map (d). The convolution works until the expected limits.

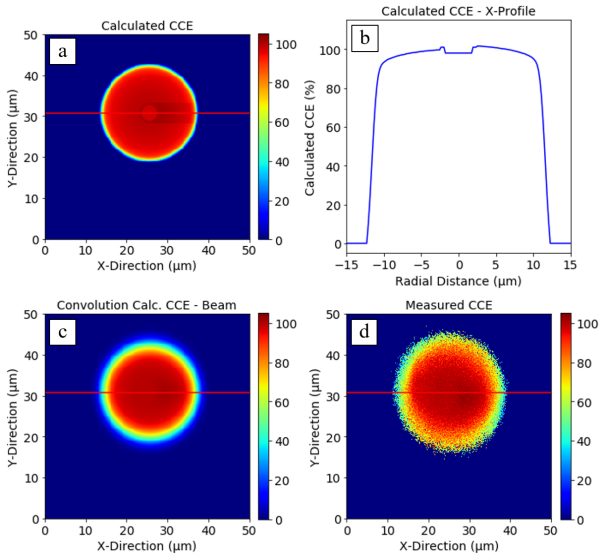

Fig. 28. (a) Calculated CCE of the detector in 2D. (b) X-profile of the calculated CCE. (c) 2D convolution of the calculated CCE with the Gaussian beam. (d) Measured CCE.

We have fitted the central region of the convolution profile to the experimental data to calculate the apparent CCE in the electrode and the Al region. In this case, the apparent CCE in the Al region is 101 %, and the central electrode has a radius of 1.9 μm and an apparent CCE of 98 %.

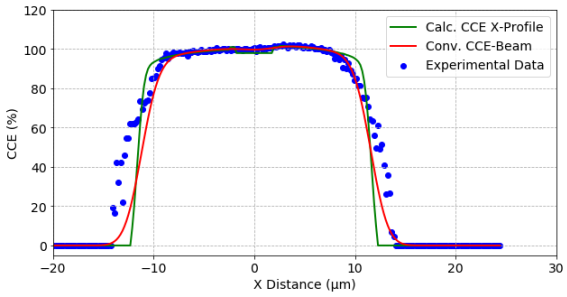

Fig. 29. X-profiles of the measured CCE, the calculated CCE, and the convolution of the calculated CCE with the beam for the 20 μm-thick microdetector.

3) Correction of the central electrode: The same way we did before, we correct the CCE in the central electrode using the apparent CCE in the Al region, obtaining a value for the real CCE in the electrode of 97 %.

Fig. 30 shows the real CCE of the 20 μm-thick microdetector after the reconstruction with the three steps.

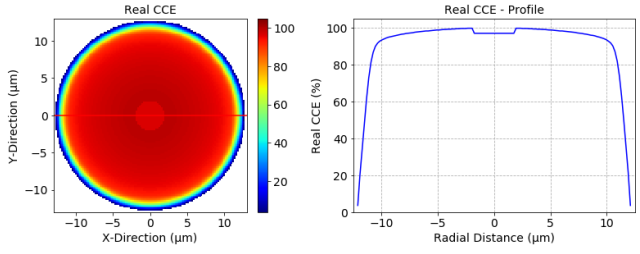

Fig. 30. Real CCE of the 20 μm-thick microdetector.

IV. Conclusion

The CCE of silicon 3D-microdetectors with two different thicknesses (10 μm and 20 μm) has been characterized by means of the IBIC technique. For both microdosimeters, the results show that the active region extends to the very edge of the detector (12.5 μm), including the n^+ diffusion region. In the region from the center up to a radial distance of 10 μm, the CCE was greater than 93 %, whereas for distances between 10 μm and 12.5 μm the mean CCE was 75 %.

the new doping process used for this second generation of microdetectors results in a more homogeneous response across the entire volume of the device

References

[1] H. H. Rossi, "Microdosimetry and the effects of small doses of radiation," *IEEE Trans. Nucl. Sci.*, vol. 23, no. 4, p. 1417–1421, Aug. 1976.

[2] C. Fleta, S. Esteban, M. Baselga, D. Quirion, G. Pellegrini, C. Guardiola, M. Cortés-Giraldo, J. G. López, M. J. Ramos, F. Gómez, and M. Lozano, "3D cylindrical silicon microdosimeters: Fabrication, simulation and charge collection study," *J. Instrum.*, vol. 10, no. 10, p. P10001, 2015.

[3] J. Prieto-Pena, F. Gómez, C. Guardiola, M. C. Jimenez-Ramos, J. Garcia-Lopez, A. Baratto-Roldán, M. Baselga, J. Pardo-Montero, and C. Fleta, "Impact of charge collection efficency and electronic noise on the performance of solid state 3d-microdetectors," *Phys. Med. Biol.*, To be published. 2020.

[4] J. Prieto-Pena, "Development of silicon sensors for dosimetry and microdosimetry," Ph.D. dissertation, Univ. de Santiago de Compostela, 2019.

[5] E. Vittone, Z. Pastuovic, P. Olivero, C. Manfredotti, M. Jaksic, A. L. Giudice, F. Fizzotti, and E. Colombo, "Semiconductor characterization by scanning ion beam induced charge (IBIC) microscopy," *Nucl. Instr. Meth. B*, vol. 266, no. 8, pp. 1312 – 1318, 2008.

[6] J. F. Ziegler, M. D. Ziegler, and J. P. Biersack, "SRIM - The stopping and range of ions in matter (2010)," *Nucl. Instr. Meth. B*, vol. 268, no. 11-12, pp. 1818–1823, Jun. 2010.

[7] M. Breese, "A review of ion beam induced charge microscopy for integrated circuit analysis," *Materials Science and Engineering: B*, vol. 42, no. 1, pp. 67 – 76, 1996, 4th International Workshop on Beam Injection Assessment of Defects in Semiconductors. [Online]. Available: http://www.sciencedirect.com/science/article/pii/S0921510796016856

[8] G. F. Knoll, *Radiation detection and measurement*, 3rd ed. John Wiley and Sons, Inc., New York, 2000.